Key Points:

- Snow cornice formation is influenced by surface shear stress and edge deposition rates
- Cornices help airborne snow particles stick to the windward side, promoting growth
- Cornice growth decreases the near-surface windward wind speed, but increases the particle collisions at the edge, promoting further growth

Correspondence to:

N. Huang and M. Lehning,
huangn@lzu.edu.cn;
michael.lehning@epfl.ch

Author Contributions:

Conceptualization: Hongxiang Yu, Guang Li
Formal analysis: Hongxiang Yu
Funding acquisition: Hongxiang Yu, Michael Lehning, Ning Huang
Investigation: Hongxiang Yu
Methodology: Hongxiang Yu, Guang Li
Software: Hongxiang Yu, Mahdi Jafari
Supervision: Michael Lehning, Jianping Huang, Ning Huang
Validation: Hongxiang Yu, Guang Li
Writing – original draft: Hongxiang Yu
Writing – review & editing: Guang Li, Mahdi Jafari, Michael Lehning, Jianping Huang

Effect of Snow Cornice Formation on Wind Fields and Snow Deposition: Insights From Numerical Simulations

Hongxiang Yu[1] , Guang Li[1], Mahdi Jafari[2], Michael Lehning[2,3] , Jianping Huang[1] , and Ning Huang[4]

[1]College of Atmospheric Science, Lanzhou University, Lanzhou, China, [2]WSL Institute for Snow and Avalanche Research SLF, Davos, Switzerland, [3]College of Architecture Civil and Environmental Engineering, Lausanne, Switzerland, [4]College of Civil Engineering and Mechanics, Lanzhou University, Lanzhou, China

Abstract Previous studies on small-scale snow cornices relied on wind-tunnel experiments to explore the suitable conditions for cornice growth. However, the absence of direct measurements of fluid and snow particle motions has limited the understanding of the mechanisms underlying snow cornice development. Here, we carried out numerical simulations under conditions identical to those of the wind-tunnel experiments. Wind profiles, snow deposition/erosion rates, surface friction velocity, and particle collision rates before and after cornice formation are quantitatively analyzed. The formation of snow cornices is primarily influenced by the shear stress on the surface, which is crucial for determining their development, while the net deposition rate on the edge plays a significant role in influencing the growth rate of these cornices. Furthermore, the analysis demonstrates that the presence of snow cornices enhances the likelihood of airborne snow particles adhering to the windward side of the edges, promoting downstream development. The growth of the snow cornice is predominantly influenced by the adhesion of settling particles at the edge, with only a small fraction of snow particles captured on the leeward side due to the effects of the return vortex (wake region). As snow cornices grow, the wind speed at the edge gradually decreases. While the collision rate of particles with the edge increases, further facilitating cornice growth. These insights contribute to a deeper understanding of snow cornice dynamics and their implications for snow stability in mountainous regions.

Plain Language Summary Wind-tunnel experiments have studied suitable wind conditions for snow cornice growth. However, our understanding of how snow cornices form has been limited due to the lack of direct measurements regarding the movement of air and snow particles. In this study, we conducted numerical simulations under the same conditions as a previous wind-tunnel experiment to analyze factors such as wind and snow distribution patterns. We found that the formation of snow cornices is primarily influenced by shear stress on their surfaces. Additionally, snow cornices play a key role in trapping airborne snow particles on the windward side, which promotes their further growth. This study focuses on numerical simulations to explore the physical mechanisms underlying snow cornice formation. Although no direct field observations are included, the fundamental physical processes of cornice growth are consistent with real-world phenomena. Therefore, the qualitative results from the simulation in this work can be used to explore the growth mechanisms of snow cornices in natural environments. Besides, the findings from this study have the potential to improve avalanche forecasting accuracy by incorporating snow cornice dynamics and improve understanding of glacier mass balance and long-term evolution.

1. Introduction

Cornice is one type of wind-driven snow patterns in cold mountain areas, and its collapse may trigger slab avalanches (Seligman et al., 1936). Understanding the causes of cornice formation is a prerequisite for predicting and preventing snow disasters. Cornice-forming process is affected by wind, air temperature, humidity, precipitation, and other environmental factors (Hancock et al., 2020; Vogel et al., 2012). The latest research has quantitatively analyzed the suitable range of wind speed for cornice growth (Yu et al., 2022). However, due to the difficulties in obtaining synchronized direct measurements of granular flow, the mechanism by which wind affects snow cornices and the feedback remains poorly understood. Specifically, previous experimental observations have shown that cornice growth is initially slow, but once a cornice forms, its growth rate accelerates rapidly, indicating a marked positive feedback effect (Yu et al., 2022). However, this kind of positive feedback in cornice development has not been previously investigated.

Snow cornices form on mountain ridges or flat terrain cliffs (Hancock et al., 2020). For a mountain ridge, the cornice growth point is the inflection point between the windward slope and leeward slope flow separation point, where the wind speed reaches the highest value (Latham & Montagne, 1970). However, the topographic effects on snow particle depositing on mountain ridges have not been fully understood (Mott et al., 2010). In numerical models, due to the limitation in mesh resolution, it is difficult to estimate the growth rate of a cornice (Latham & Montagne, 1970). For a flat terrain cliff, the cornice growth point is the inflection point between the flat surface and the leeward slope separation point. This flowing pattern can be considered as a Backward-Facing Step flow. Previous research has primarily focused on snow deposition over the step (Lu & Zhang, 2019; Zhang et al., 2023), but deposition on the step edge has not been studied in detail, which is however a critical growth mechanism, especially in the initial stage of snow cornice formation. From the previous wind-tunnel experiment of Yu et al. (2024), it is observed that in addition to the direct deposition mode, some snow particles may also undergo backsorption on the cliffs or the leeward side of the snow cornice. However, the collision rates of particles on the windward and leeward sides of the edge have never been quantified.

To our knowledge, there is still no numerical model that can well simulate the growth of a cornice. This limitation arises not only from low mesh resolution but, more critically, from the absence of effective parameterization for particle adhesion at the edge. The probability for airborne particles to adhere to the edge is determined by the product of the particle-surface colliding frequency and particle fast-sintering rate. The particle fast-sintering rate is related to air temperature and humidity (Bahaloo et al., 2022; Szabo & Schneebeli, 2007), and the particle-surface colliding frequency to the physical properties of snow particles such as shape, density, dendrites number, impact velocity/angle, restitution coefficient, and fluid properties. Measuring the collision frequency at the edge directly from the experiment is challenging, so quantitative numerical simulations are needed to study the adhesion probability of snow particles in that area.

In this work, we carried out numerical simulations using the Eulerian-Lagrangian method to reproduce our earlier wind-tunnel experiments on cornice formation. We also calculated variables that were not measured in the wind-tunnel experiments, as explained in detail later in Section 3. Through the analysis of the numerical results, we examined the fluid field and particle deposition patterns before and after the cornice formation, as well as the collision frequency at the edges. This study enhances our understanding of the mechanism underlying snow cornice growth from the dynamic physical perspective of wind-blown snow.

2. Numerical Model

The simulation is based on the model of snowBedFoam 1.0 (Hames et al., 2021) developed at the École Polytecnique Fédérale de Lausanne, which is a physically-based Eulerian-Lagrangian snow transport model implemented in the open source fluid dynamics software OpenFOAM (https://www.openfoam.com (OpenCFD, 2021)). To simulate aeolian snow transport, snowBedFoam 1.0 employs coupled Eulerian-Lagrangian phases, where a finite number of snow particles are dispersed within a continuous air phase. Snow erosion and deposition processes are represented through physics-based equations, similar to those used in the well-established LES-Lagrangian Stochastic Model (Comola & Lehning, 2017; Melo et al., 2022; Sharma et al., 2018). Due to its computational intensity, this approach is best suited for simulating snow movement and distribution over small-scale terrain.

2.1. Governing Equations for Fluid Phase

The continuity equation and momentum equation for incompressible flow with snow particles can be expressed as follows:

$$\frac{\partial u_i}{\partial x_i} = 0 \tag{1}$$

and

$$\frac{\partial u_i}{\partial t} + \frac{\partial u_i u_j}{\partial x_j} = -\frac{1}{\rho}\frac{\partial p}{\partial x_i} + \nu \frac{\partial^2 u_i}{\partial x_i \partial x_j} + F_i \tag{2}$$

where t is time, ρ is air density, p is pressure, ν is kinematic viscosity, u_i is the component of the velocity vector $\vec{u}$ and x_i is the spatial coordinate extended to x, y, and z. F_i is the collective feedback force of all snow particles within a grid cell acting on the fluid, which is calculated as the summation of the drag forces on snow particles:

$$F_i = -\Sigma_{j=1}^{jj} F_d(j) = -\Sigma_{j=1}^{jj} \frac{1}{2} C_D A |u_f - u_p(j)|(u_f - u_p(j)) \tag{3}$$

in which jj is the sum number of particles in a single cell, A is the effective cross-sectional area of an individual particle, u_f the fluid velocity, u_p is the particle velocity, and C_D is the drag coefficient defined as (Anderson & Haff, 1991a):

$$C_D = \begin{cases} \frac{24}{Re}\left(1 + \frac{1}{6}Re^{\frac{2}{3}}\right) & Re > 1000 \\ 0.424 & Re \leq 1000 \end{cases} \tag{4}$$

2.2. Governing Equations for Particle Phase

In the equation of particle motion, gravity, buoyancy and drag forces are considered.

$$m_p \frac{du_p}{dt} = \frac{1}{6}\pi(\rho_p - \rho_a)d^3 g - \frac{1}{2}C_D A|u_f - u_p|(u_f - u_p) \tag{5}$$

in which, m_p is the particle mass, ρ_p is the particle density, ρ_a is the air density, d is particle diameter.

Moving snow particles are subjected to gravity and fall at a certain velocity. Once they impact the surface, they either rebound or deposit on the snow surface, contributing to snow accumulation. Additionally, the collision can result in a splash effect, where smaller particles are ejected into the air, affecting snow distribution and influencing snow patterns (Clark et al., 2011). In this simulation, the probability for a particle rebound after the impact with the snow model is calculated by (Groot Zwaaftink et al., 2013):

$$P_r = P_m(1 - e^{-\gamma v_i}) \tag{6}$$

where v_i is the particle impact velocity, and P_m is the maximum rebound probability. The particle rebound velocity is assumed to be $0.5v_i$ (Doorschot & Lehning, 2002), and the rebound angle obeys an exponential distribution (Kok & Renno, 2009). The number of ejected particles $N = \min(N_E, N_M)$, in which N_E is estimated via the momentum equation N_M and energy equation (Comola & Lehning, 2017):

$$N_E = \frac{(1 - P_r \epsilon_r - \epsilon_{fr})d^3 v_i^2}{2\langle v \rangle^2 \left(\langle d \rangle + \frac{\sigma_d^2}{\langle d \rangle}\right)^3 \left(1 + r_E\sqrt{5\left[1 + \left(\left(\frac{\sigma}{\langle d \rangle}\right)^2\right)^9\right] - 5}\right) + 2\frac{\phi}{\rho_P}} \tag{7}$$

$$N_M = \frac{\left(1 - P_r \mu_r - \mu_{fr}\right)d^3 v_i \cos\alpha_i}{\langle v \rangle^2 \left(\langle d \rangle + \frac{\sigma_d^2}{\langle d \rangle}\right)^3 (\langle \cos\alpha \rangle \langle \cos\beta \rangle r_M \sqrt{\left[1 + \left(\frac{\sigma_d}{\langle d \rangle}\right)^2\right]^9} - 1)} \tag{8}$$

where ϵ_f and ϵ_r are the kinematic energy lost and preserved after the particle-bed surface collision respectively, μ_f and μ_r are the kinematic energy fractions, $\langle d \rangle$ is the average value of particle diameter, σ_d is the standard deviation of the particle diameter, $\langle v \rangle$ is the average velocity of particles ejected with vertical angle α and horizontal angle β, ϕ is the snow bed cohesion energy, r_E is the coherence coefficient of the ejected particle mass m and the square of its velocity v^2, r_M is the coherence coefficient of ejected particle mass m and velocity v.

Table 1
Model Parameters

Variable	Value
Roughness length	10^{-5} m
Kinetic viscosity ν	1.13×10^{-5} m^2 s^{-1}
Air density	1.41 kg m^{-3}
Wind speed	3.5–6 m s^{-1}

2.3. Domains and Simulation Setup

The domain of the simulation is a wind tunnel geometry with 2.2 m in streamwise, 1.2 m in spanwise, and 0.5 m in height, which is 1:1 as in the previous experiment (Yu et al., 2022). The structured hexahedra mesh consists of 106 cells, with a uniform and orthogonal arrangement ensuring numerical stability and high accuracy. The mesh, with acceptable non-orthogonality (maximum 17.2), aspect ratio (maximum 1.8), and skewness, is well-suited for high-precision numerical simulations (Table 1).

For the flow phase, the inlet is set as a patch with a boundary condition of constant flow velocity, which drives the flow into the domain. The outlet is set as a patch as well, with a zero-gradient boundary condition. The wind tunnel inner side, outer side wall, upper wall, and lower wall are all set as walls, which are treated as no-slip and impermeable. The fluid parameters are shown as Table 1. For the particle phase, snow particles are injected from the round area at the top wall of the wind tunnel, as shown in Figure 1. The seeding rate is a constant of 0.007 kg s^{-1}. The circle sieve-shaped seeding port in the numerical domain is in the same position on the top wall of the wind tunnel in the experiment with an identical area size (Yu et al., 2022). The particle properties used in simulations are listed in Table 2. The snow model is defined as a snow bed boundary with particle-bed interactions. Splash functions developed by (Comola & Lehning, 2017) are implemented to describe the particle-bed interactions, which govern processes like particle deposition, rebound, or splash. The outlet is set as an escape boundary. All other faces of the wind tunnel are set as rebound boundaries, meaning particles colliding with these walls will rebound elastically.

In the field, cornices can form on two types of geometries: mountain edges and mountain ridges, with the key difference being whether there is a flat surface before the cliff (Seligman et al., 1936). Experiments show that the growth rate of snow cornices is faster on mountain edges, making this geometry more suitable for study (Yu et al., 2022). To remain consistent with the previous wind tunnel experiment, the mountain edge was selected as the simulation model. Two geometries are chosen, which represent before and after cornice formation. Before cornice formation, the geometry is an edge-shaped model of the same size as the snow model in the experiment. The second geometry includes a wedge-shaped cornice horizontally hanging at the edge, with a length of 0.145 m, which is the maximum cornice length observed in the previous wind tunnel experiment.

In the simulation, Reynolds-Average Navier-Stokes method is applied to have a time-averaged momentum equation for the continuum phase (air). Therefore, for the turbulence closure, the two-equation turbulence model of $k - \epsilon$ is chosen to obtain the turbulent viscosity. The initial time step (ΔT) is set to 1×10^{-5} s, with dynamic time step adjustment enabled to ensure numerical stability, and the maximum Courant number is set as 1. This setup allows the time step to be automatically optimized during the simulation process. Different solution strategies are applied based on the characteristics of each variable: an efficient algorithm is used for pressure to achieve rapid convergence, while smooth solving methods are adopted for velocity and turbulence-related variables to ensure stability. Additionally, an iterative process is employed to couple pressure and velocity, ensuring
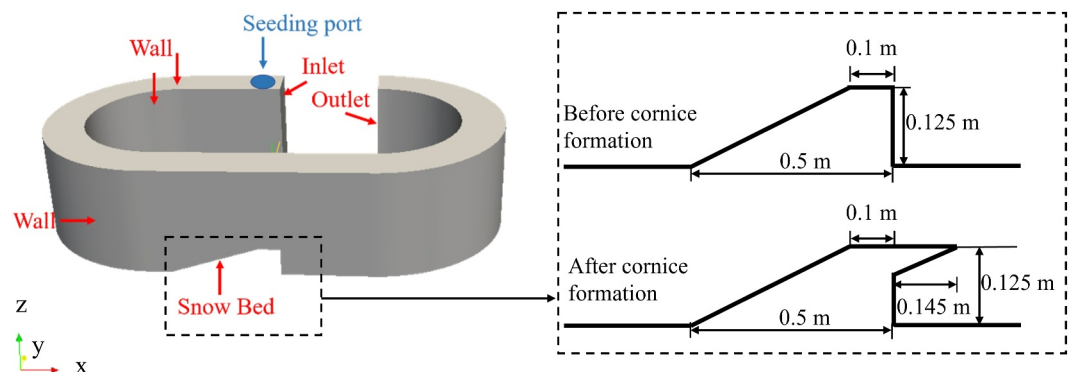

Figure 1. Schematics of simulation domain and snow model.

Table 2
Particle Information

Variable	Value
Snow model particle mean diameter	0.5 mm
Snow model particle minimum diameter	0.05 mm
Snow model particle maximum diameter	1 mm
Particle density(ice)	900 kg m^{-3}
Seeding rate	0.007 kg s^{-1}
Seeding particle diameter	0.5 mm
Seeding time	30 s

consistency and accuracy in the simulation of transient flows. Furthermore, second-order interpolation is used in the simulation to precisely capture the distribution of flow field variables.

2.4. Model Verification

To verify the simulation results of the wind field, wind profiles of nine points distributed in both streamwise and spanwise directions within the working section of the wind tunnel are compared with the experimental measurement results (Sommer et al., 2017), as shown in Figure 2a. This comparative analysis between measured and simulated wind profiles is crucial for ensuring the accuracy and reliability of our simulations. The measured and simulated wind profiles at upstream, middle, and downstream points are presented in Figures 2b–2d, respectively. In these figures, the lines represent simulation results, while the dots represent the observation results. The colors black, red, and blue represent data collected from the inner, center, and outer sides of the wind tunnel, respectively. Here, U denotes the wind velocity recorded by the wind sensor installed on the upper wall of the wind tunnel, while the reference velocity U_{ref} corresponds to the wind speed that is set as the average input velocity before the experiment begins. This value is for establishing consistent flow conditions, allowing for comparisons of aerodynamic forces acting on the test subject throughout the experiment. The velocity acceleration ratio is defined as U/U_{ref}, and the vertical profile of this ratio is consistent with the experimental measurements.

Analysis of the correlation coefficient shows that, R at all locations exceed 0.93, suggesting a high degree of consistency between simulated and measured wind profiles. Overall, the simulation captures the main
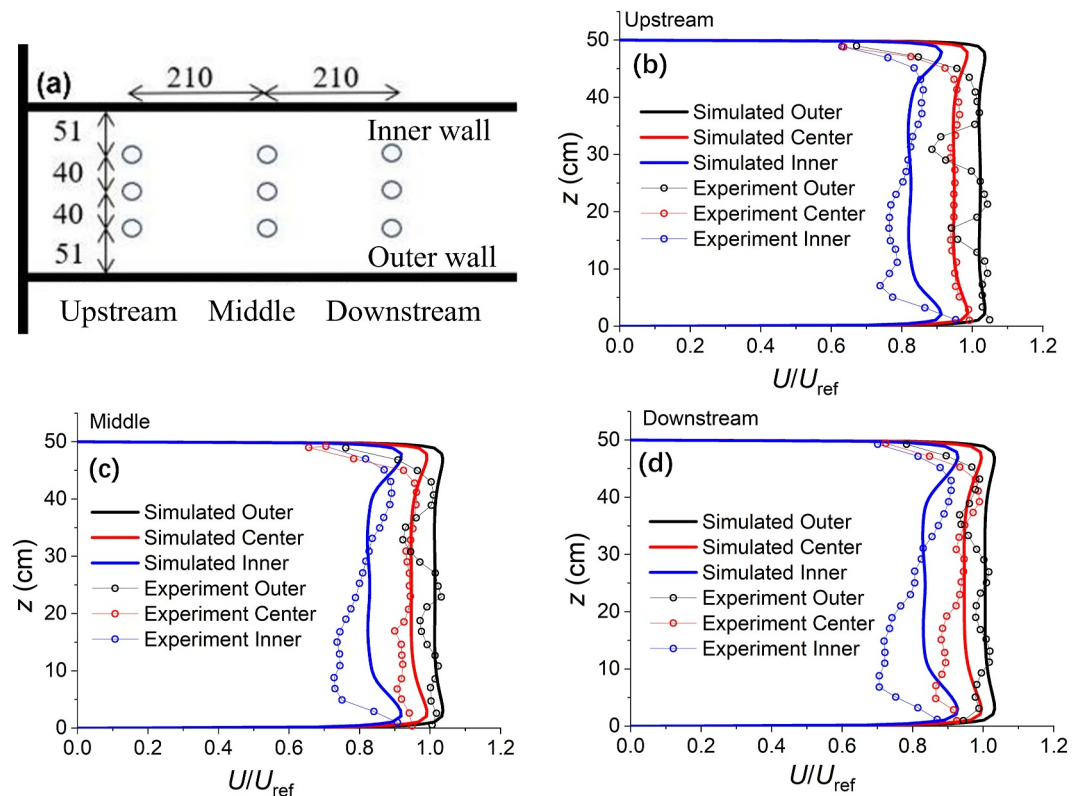

Figure 2. (a) Schematic of measurement positions in wind tunnel test section, showing nine discrete points arranged streamwise and spanwise to capture wind speed profiles. Non-dimensional wind profiles in (b) upstream, (c) middle, and (d) downstream regions are shown in dotted lines for experiment measurement and solid lines for simulation results. The reference wind speed is $U_{ref} = 3$ m s^{-1}.
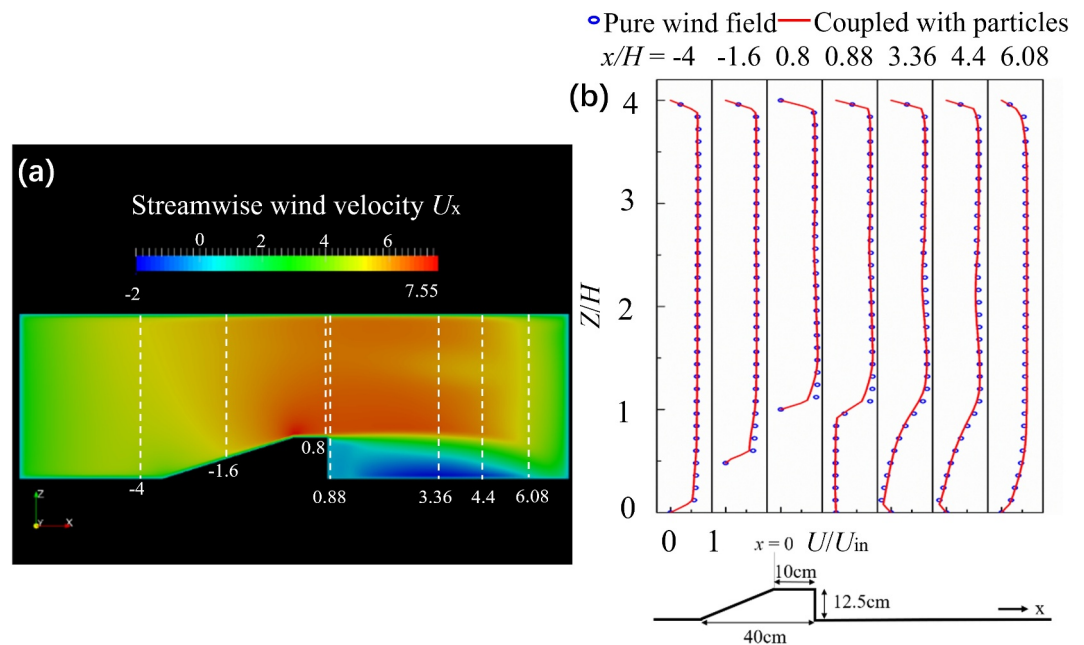
Figure 3. (a) Streamwise wind velocity contour at the center cross-section of the straight section in the wind tunnel at stable state. The white dashed lines indicate the positions corresponding to the extracted wind profiles. (b) Non-dimensional wind profiles at different x/H in streamwise. The inlet wind speed is $U_{in} = 4.5$ m s^{-1}.

characteristics of the measured wind profiles, particularly in the core flow region, and fulfills the general requirements for wind tunnel model validation.

Both the wind-tunnel experiment and simulation results indicate that the wind field inside the wind tunnel is nearly uniform, with a boundary layer thickness of approximately 2 cm. Still, discrepancies do exist, particularly for the measurements at the inner side of the downwind area. In our simulation, wind speed is maintained as a constant at the inlet, while in the experiment, wind propellers installed within the wind tunnel generate the airflow. This difference results in less uniform wind profiles in the experimental results, influenced by the effects of inertial forces.

3. Results and Discussion

3.1. Wind Field Characteristic

In the experiment of Yu et al. (2022), wind field over snow cornice was not measured, which limited the analysis of the interaction between snow cornice formation and the wind field. Here, we first take the case where the inlet wind speed U_{in} is set to 4.5 m s^{-1}, as illustrated in Figure 3a, which shows the streamwise wind field before the cornice formation. The airflow accelerates over the windward side of the model and undergoes separation at the sharpest point (edge) as a result of pressure differences induced by changes in the cross-sectional area. We define the non-dimensional wind speed as U/U_{in}, where U is the wind speed. z/H is the dimensionless height, in which z is height above the surface and $H = 0.125$ m is the model height. x/H is the normalized streamwise position, and x is the distance from the corner between the slope and the flat surface. Non-dimensional wind profiles at different measuring points in the streamwise direction are shown in Figure 3b. The red line is the wind profile of the flow field with particles, and the blue circle is that with no particles. As seen, as particles above the ground extract momentum from the flow, the wind speed is lower in the first case. The wind speed is lower close to the ground and in particular over the snow model because of the momentum loss caused by the airborne snow particles. A zone of low wind speed (shown in blue) is observed in the wake, located downwind of the model and below the model height. The low-speed region consists of a vortex between $x/H = 3.36$ and 6.08, in which $x/H = 3.36$ is the reversal starting point where the streamwise wind speed U_x starts to have negative values. $x/H = 6.08$ is the reattachment point where U_x at $z/H = 0.04$ starts to be positive again.

3.2. Deposition and Erosion Rate

The deposition rate q_{dep} is determined by counting the number of impinging particles that, upon collision with the snow surface, exhibit a rebound velocity of zero within each surface cell over a unit time interval.

$$q_{dep} = \Sigma_{j=1}^{m} \Sigma_{i=1}^{n} \frac{1}{6}\pi d_p{}^3 \rho_p \tag{9}$$

in which, m is the cell number on the snow surface, and n is the total number of particles within a surface cell.

From the previous experimental observation, there are three particle sources that contribute to forming the snow cornice (Yu et al., 2022). The first is the seeding grains depositing directly to the edge. The second is the transport of the rebounding particles when the wind speed is above the rebound threshold, and the third is the resuspension of the deposited particles due to the aerodynamic entrainment when the wind speed is above the fluid threshold. In the previous experiment, we employed a snow model consisting of compacted snow. To maintain consistency with the experimental conditions, we did not activate the aerodynamic entrainment module during the simulation. Nevertheless, it is important to note that aerodynamic entrainment may still occur following the deposition of fresh snow on the snow model. To accurately quantify this entrainment effect, we utilized the same formula implemented in the aerodynamic entrainment module to calculate the potential mass loss from the snow model. The potential erosion rate q_{ero} is calculated based on the friction velocity value (Anderson & Haff, 1991b):

$$q_{ero} = \frac{C_e}{8\pi\langle d_p\rangle^2}(\tau_s - \tau_{th})\Delta x \Delta y m_p \tag{10}$$

where $C_e = 0.45$ is constant, $\langle d_P \rangle$ is mean particle diameter, Δx and Δy are the cell grid sizes in streamwise and spanwise separately, m_P is the mass of the particle, and τ_{th} is the threshold shear stress which can be expressed as:

$$\tau_{th} = u_{*th}^2 \rho_a \tag{11}$$

where u_{*th} is the threshold friction velocity and ρ_a is the air density. The threshold friction velocity is assumed to be equal to the threshold aerodynamic entrainment friction velocity $u_{*th} = u_{*th}^{ae} = 0.17$ m s^{-1} (Nemoto & Nishumura, 2001). In Equation 10, τ_s is the surface shear stress which can be expressed as (Bagnold, 2012):

$$\tau_s = u_*^2 \rho_a = \left(\frac{k|U|}{\ln(z/z_0)}\right)^2 \rho_a \tag{12}$$

where U is the wind speed at the height z, $k = 0.41$ is von Kármán constant, ρ_a is the air density, and u_* is the surface friction velocity which can be calculated. The friction velocity u_* increases along the windward slope and reaches the maximum on the flat surface, as shown in Figure 4a.

In the experiment, the measured threshold value of rebound wind speed at the height of the MiniAir sensor is 3.2 m s^{-1}, which is the lower limit wind speed of forming a stable saltation layer in the wind tunnel (Yu et al., 2022). Correspondingly, the calculated surface friction velocity at the edge in the case of $U = 3.2$ m s^{-1} is defined as threshold rebound friction velocity $u_{*th}^{re} = 0.14$ m s^{-1}. This value represents the threshold at which particles begin to be entrained from the surface due to the splashing process caused by other particles. As shown in Figure 4b, the surface friction velocity u_* on the snow model is higher than the rebound threshold u_{*th}^{re} (shown in dash dot line), which indicates that there is a stable saltation layer when $U > 3.2$ m s^{-1}, in consistency with the wind-tunnel experiment. On the other hand, for newly deposited snow particles, surface erosion occurs where the surface friction velocity u_* is higher than the threshold aerodynamic entrainment friction velocity $u_{*th}^{ae} = 0.17$ m s^{-1}. By comparing u_* (dots in Figure 4b) with u_{*th}^{ae} (dash line in Figures 4b–4c), it can be inferred that: (a) on flat surface: erosion occurs for all wind conditions (3.5–6 m s^{-1}); (b) on the windward slope surface: as wind speed increases, the erosion area on the windward slope surface enlarges, and when the wind speed is at 5.5–6 m s^{-1}, erosion affects the entire windward slope surface; and (c) at the edge: erosion occurs when the wind speed is greater than $U > 4$ m s^{-1}.
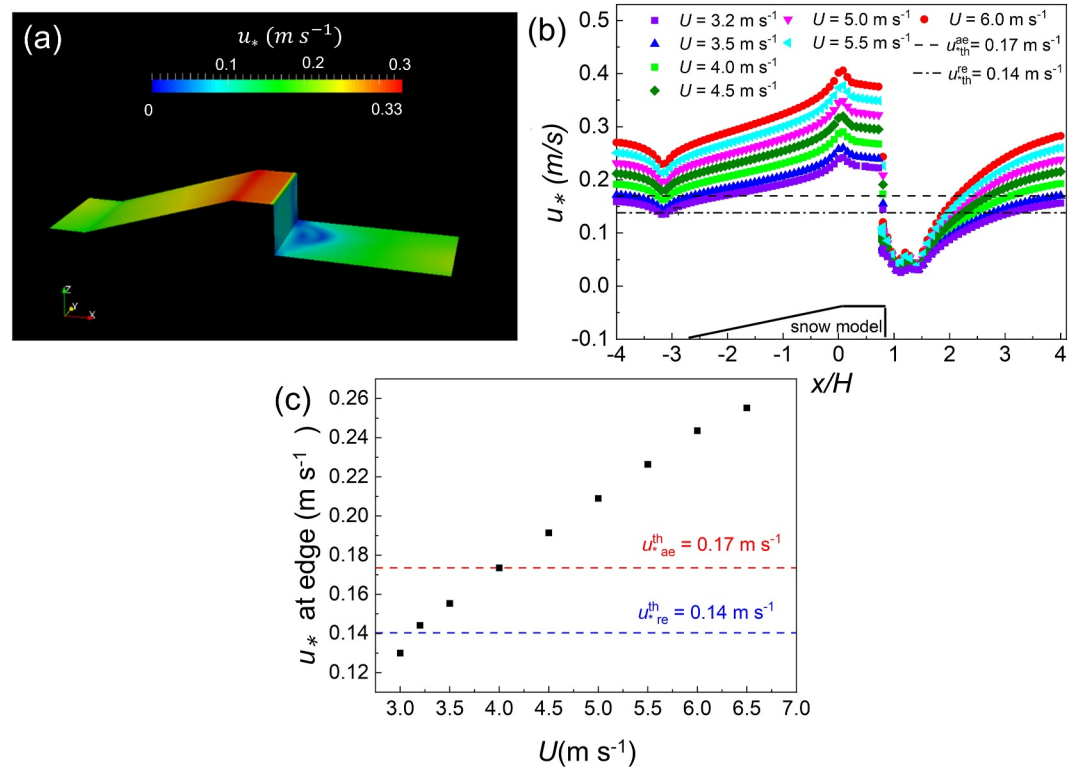
Figure 4. (a) Friction velocity on the snow model; (b) Friction velocity along the center line of the snow model; and (c) Friction velocity at the edge of the snow model before cornice formation. u_{*th}^{ae} is the threshold value of aerodynamic entrainment velocity, and u_{*th}^{re} is the threshold rebound velocity.

As shown in Figure 5a, under weak wind conditions, most particles deposit at the beginning ($x/H = -3$) of the windward side of the snow model. Under stronger wind conditions, snow particles are more evenly deposited downstream on the windward slope. The erosion rate q_{ero} progressively increases with wind speed, reaching its maximum value at the corner where the windward slopes meet the flat surface, indicating that erosion is most likely to occur at this specific point on the snow model. To evaluate the competing effects of deposition and erosion on cornice growth, we utilized the net deposition rate to estimate the mass balance on the snow model surface, as illustrated in Figure 5b. The net deposition rate value at the edge ($x/H = 0.8$) is depicted in the locally enlarged image, indicating that the maximum net deposition rate occurs at moderate wind speed ($U = 4.5$–5 m s^{-1}), while the minimum net deposition rate are observed under weak wind ($U = 3.5$ m s^{-1}) and the strong wind ($U = 6$ m s^{-1}).
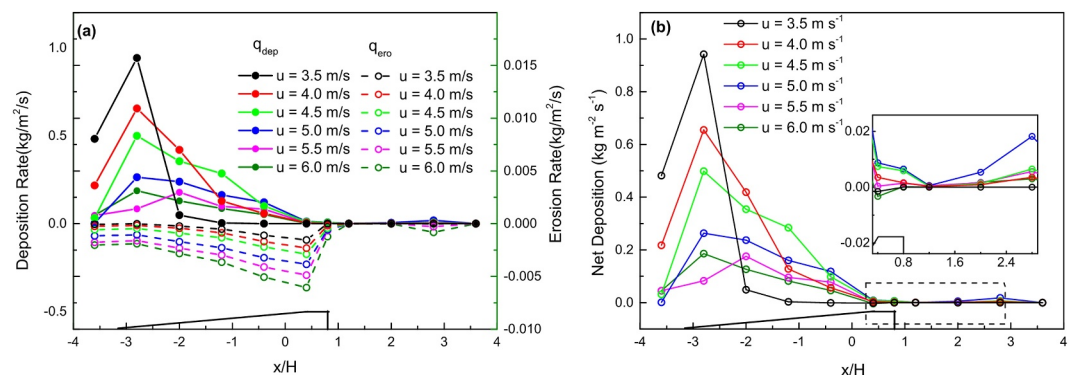

Figure 5. (a) Deposition and erosion rates and (b) net deposition rate along the ridge at the center under various wind conditions with a local enlarged image.
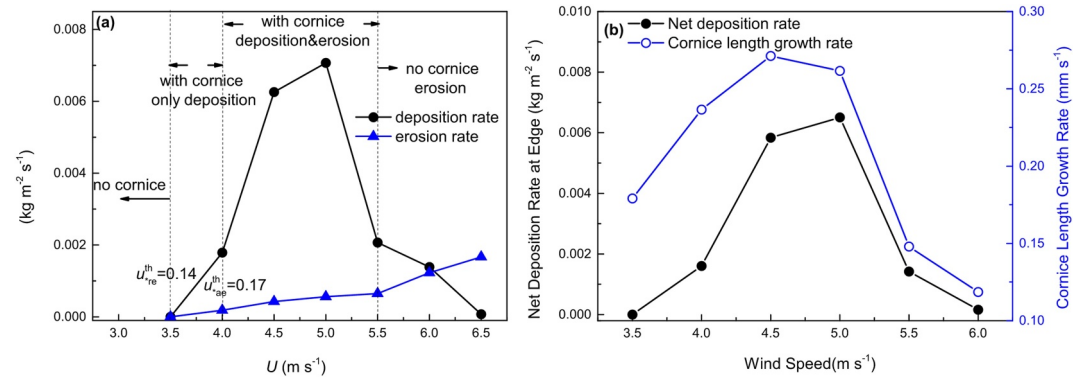
Figure 6. (a) Absolute value of deposition and erosion rate at the edge of the model in different wind conditions. (b) The net deposition rate and cornice length growth rate comparison.

The net deposition rate is defined as the sum of the deposition rate and erosion rate. As illustrated in Figure 6a, for $U < 3.5$ m s^{-1} ($u_* < u_{*th}^{re}$), no cornice forms due to insufficient mass in the saltation layer. For 3.5 m s^{-1} $\leq U < 4$ m s^{-1} ($u_{*th}^{re} < u_* < u_{*th}^{ae}$), the cornice forms primarily due to deposition. For 4 m s^{-1} $\leq U \leq 6$ m s^{-1} ($u_* \geq u_{*th}^{ae}$), erosion starts to effect on the surface accumulation at the edge. The source of material for cornice growth comprises both deposition and erosion. However, for $U > 6$ m s^{-1}, the deposition rate becomes less than the erosion rate at the edge, resulting in no cornice formation. As shown in Figure 6b, the net deposition rate reaches its maximum value at wind speeds of 4.5–5 m s^{-1}.

3.3. Feedback of Cornice on Wind Field, Particle Motion, and Cornice Growth at the Tip

After the cornice reaches the maximum length (average value observed in the experiment is 0.145 m), the flow field changes first due to the morphological alterations of the snow model. The streamwise velocity contour along the central line of the wind tunnel is depicted in Figure 7a. Similar to the conditions before cornice formation, the streamwise velocity reaches its maximum at the corner of the windward slope, with a low-speed vortex zone located downstream of the edge (indicated in blue). The dimensionless wind speed profiles at various positions in
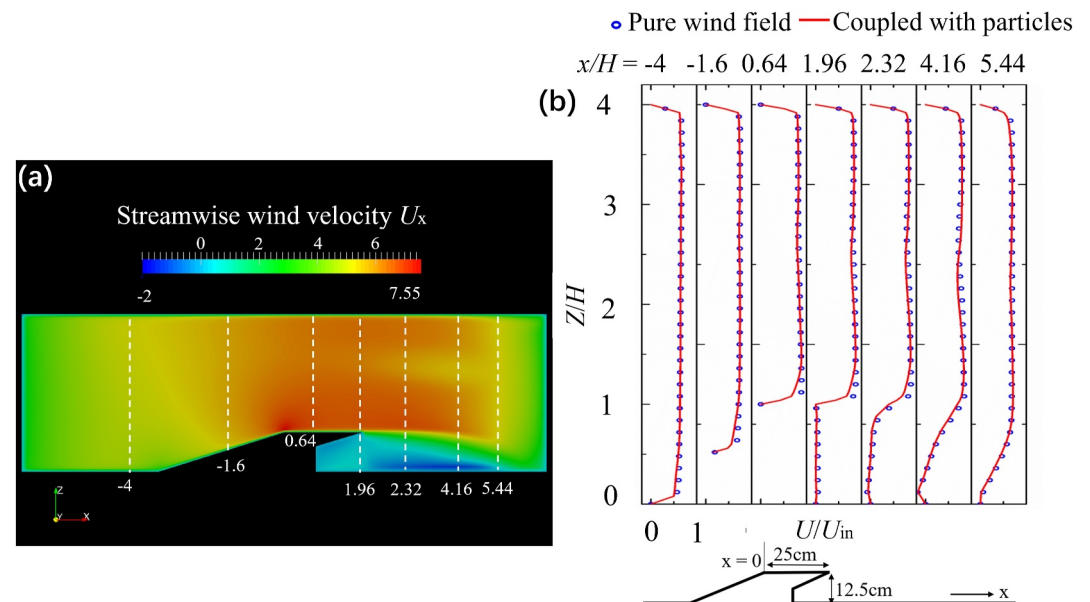

Figure 7. (a) Streamwise wind velocity contour at the center cross-section of the straight section tunnel at the stable state. The white dashed lines indicate the positions corresponding to the extracted wind profiles. (b) Non-dimensional wind profiles at different x/H in streamwise. The inlet wind speed is $U_{in} = 4.5$ m s^{-1}.
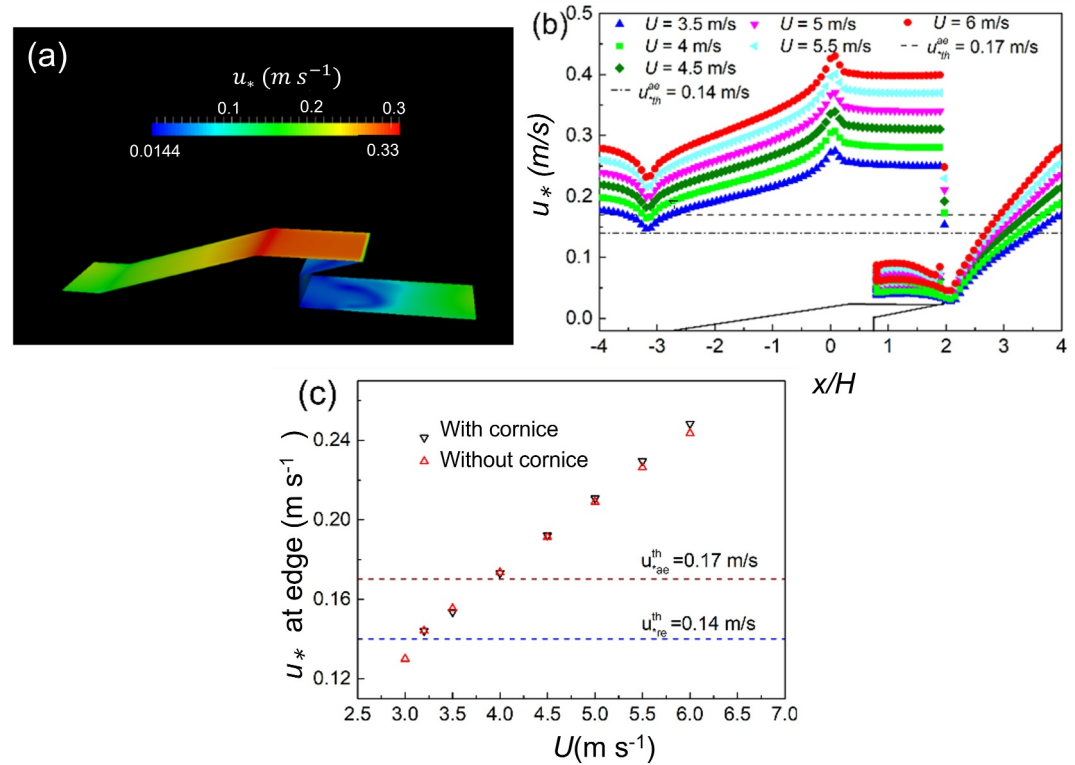
Figure 8. (a) Friction velocity on the snow model; (b) Friction velocity along the center line of the snow model; and (c) Friction velocity at the edge of the snow model after cornice formation. u_{*th}^{ae} is the threshold value of aerodynamic entrainment velocity, and u_{*th}^{re} is the threshold rebound velocity.

the streamwise direction are presented in Figure 7b. The near-surface streamwise wind speed becomes negative at $x/H = 2.3$ and returns to a positive value at $x/H = 5.4$. Consequently, the reverse vortex is positioned between $x/H = 2.3$ and 5.4, closer to the edge than its position before cornice formation, exhibiting a length that is 14.7% longer than before.

The trend in surface friction velocity variation is consistent with the conditions before cornice formation. As shown in Figures 8a and 8b, the surface friction velocity increases along the windward slope and displays a sudden decrease on the cornice tip. The magnitude of friction velocity u_* is slightly lower after the cornice forms compared to before its formation, as is shown in Figure 8c.

Particle trajectories are shown in Figure 9. Before the cornice formation, most particles collide with the snow surface on the windward slope. Few particles collide with the flat surface and rush out to the edge with streamwise velocity, instead of stopping at the edge. After the cornice formation, the colliding frequency of particles on a flat surface increases, especially at the edge. This might be because, after a snow cornice formation, particles experience more collision times with the flat surface and lose a portion of momentum and mass, which provides more favorable conditions for stopping at the edge.

To quantitatively investigate the colliding frequency of particles at the edge, the colliding frequencies of particles on the windward and leeward sides of the edge is then analyzed. On the windward side, the collision frequency is about 10 times higher than that on the leeward side, and the collision frequency at the edge reaches the highest value before the cornice formation when $U = 4.5$ m s^{-1}. After cornice formation, the maximum frequency shifts to 5 m s^{-1}, as is shown in Figure 10a. On the leeward side, before the cornice formation, the maximum colliding frequency occurs at $U = 4.5$ m s^{-1}. While after cornice formation, the maximum colliding frequency shifts to $U = 5$ m s^{-1}, as is shown in Figure 10b.

From the analysis above, it can be concluded that cornice formation alters the surrounding flow conditions, including local wind speed and vortex position, both of which influence particle trajectories. Cornice formation
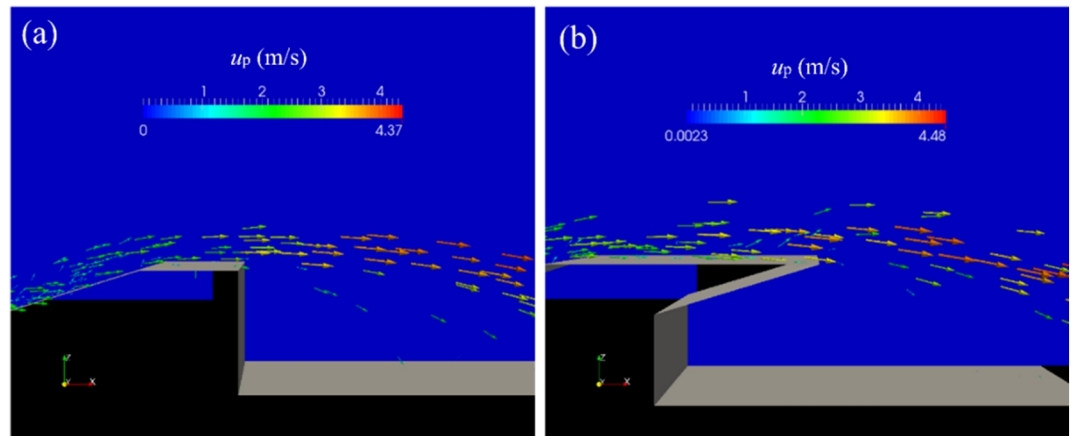
Figure 9. Particle velocity vectors for the case (a) before the cornice formation and (b) after the cornice formation.

increases the collision probability of snow particles with the windward side of the tip, thereby promoting the cornice's development in length and thickness. The growth of the snow cornice primarily relies on the settling adhesion of particles at the edge or on the windward side of the tip, with only a small portion of the snow particles adhering to the leeward side at the edge and the cornice.

It should be noted that the Reynolds number of the original numerical simulation model is $\mathrm{Re} = 1.3 \times 10^5$ on average, which falls within the self-similar region $\left(10^5 \leq \mathrm{Re} \leq 10^8\right)$. In this range, the turbulence characteristics of the flow field and the velocity profile remain unchanged even if the size of the simulation domain is adjusted. Thus, in this work, dynamic similarity is ensured, and the critical physical quantities, such as friction velocity, remain unaffected by the domain size.

4. Conclusions

To further understand the intrinsic physical mechanisms of snow cornice formation and growth, this work conducted numerical simulations to investigate the airflow and particle moving characteristics before and after snow cornice formation. The simulated results are consistent with the previous wind-tunnel experiments, confirming the reliability of our numerical model. Moreover, the simulation results allowed us to obtain information that was not directly accessible through previous experiments. We found that cornice formation is a comprehensive process involving both deposition and erosion. The shear stress on the surface determines whether a snow cornice forms, while the net deposition rate on the edges dictates the wind speed at which the growth rate of the cornice increases. The lower threshold wind speed for snow cornice formation corresponds to the threshold
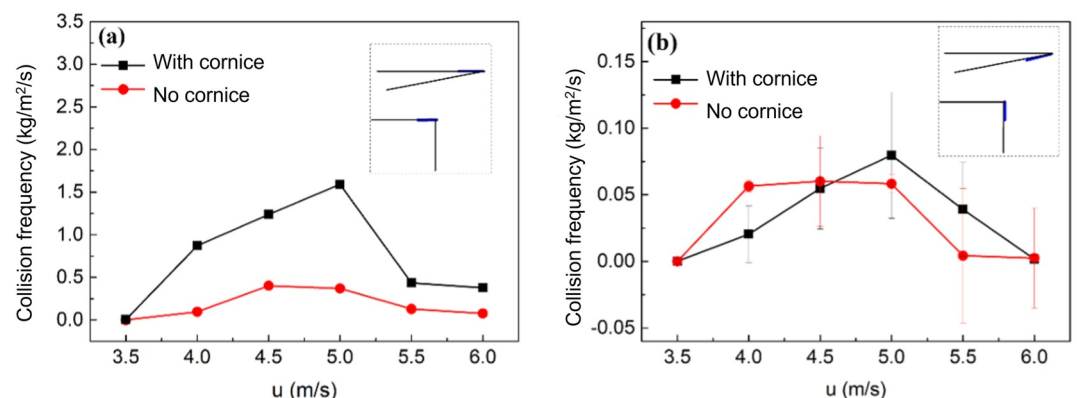

Figure 10. Particle collision frequency on (a) windward and (b) leeward of the edge before and after cornice formation. The error bars in (b) show the standard deviation of the collision rate over the last 50 s in steady state.

rebound wind speed of snow particles, which influences the formation of a saltation layer. The upper critical wind speed occurs when the net deposition rate reaches zero.

Previous experimental observations indicate that cornice growth is slow at the initial state; once a cornice appears, its growth rate accelerates rapidly (Yu et al., 2022). Our simulation results explain this positive feedback mechanism: cornice formation locally reduces wind speed at the edge and increases the particle collision frequency at the edge, making snow particles more likely to adhere to the edge after the cornice has formed. The growth of the snow cornice primarily relies on the settling adhesion of particles at the windward side of the edge, with only a small fraction of snow particles being absorbed on the leeward side through the return vortex.

Although our simulation results provide quantitative insights into the mechanism of snow cornice growth, the model has limitations in directly comparing with field observations due to the complex environmental conditions in nature, such as strong intermittency of wind flow and complex terrain. Our simulation results can qualitatively capture the essential physical mechanisms governing snow cornice formation observed in the field. The primary flow characteristics and wind speed range for cornice formation remain unaffected by domain scaling in our simulations. However, for quantitative accuracy, further calibration and validation with further field observation data are required. Therefore, high-resolution field observation data are essential to bridge the gap between small-scale simulations and large-scale mountain terrains, and this will be the focus of our future research. Building upon this, the acquisition of detailed field data will not only facilitate model validation but also lay the groundwork for more comprehensive predictions and practical applications.

In future work, we intend to predict snow cornice growth in the mountainous terrain under various conditions, such as different wind fields, precipitation strength, and terrain conditions. This will enable the development of a parameterization scheme for snow cornice growth, which can be incorporated into avalanche models to improve forecasting accuracy. Additionally, the findings of this study, incorporating wind-snow feedback mechanisms, provide valuable insights and references for glacier and ice flow modeling work.

Data Availability Statement

The code in this work is available via (Hames et al., 2021). Data archiving is available at Zenodo (Yu, 2024).

References

Anderson, R. S., & Haff, P. K. (1991a). Wind modification and bed response during saltation of sand in air. *Acta Mechanica*, 21–51. https://doi.org/10.1007/978-3-7091-6706-9_2

Anderson, R. S., & Haff, P. K. (1991b). Wind modification and bed response during saltation of sand in air. In *Aeolian grain transport 1* (pp. 21–51). Springer.

Bagnold, R. A. (2012). The physics of blown sand and desert dunes. *Courier Corporation*.

Bahaloo, H., Eidevåg, T., Gren, P., Casselgren, J., Forsberg, F., Abrahamsson, P., & Sjödahl, M. (2022). Ice sintering: Dependence of sintering force on temperature, load, duration, and particle size. *Journal of Applied Physics*, *131*(2), 025109. https://doi.org/10.1063/5.0073824

Clark, M., Hendrikx, J., Slater, A., Kavetski, D., Anderson, B., Cullen, N., et al. (2011). Representing spatial variability of snow water equivalent in hydrologic and land-surface models: A review. *Water Resources Research*, *47*(7), W07539. https://doi.org/10.1029/2011WR010745

Comola, F., & Lehning, M. (2017). Energy- and momentum-conserving model of splash entrainment in sand and snow saltation. *Geophysical Research Letters*, *44*(3), 1601–1609. https://doi.org/10.1002/2016GL071822

Doorschot, J., & Lehning, M. (2002). Equilibrium saltation: Mass fluxes, aerodynamic entrainment, and dependence on grain properties. *Boundary-Layer Meteorology*, *104*(1), 111–130. https://doi.org/10.1023/A:1015516420286

Groot Zwaaftink, C., Cagnati, A., Crepaz, A., Fierz, C., Macelloni, G., Valt, M., & Lehning, M. (2013). Event-driven deposition of snow on the Antarctic plateau: Analyzing field measurements with snowpack. *The Cryosphere*, *7*(1), 333–347. https://doi.org/10.5194/tc-7-333-2013

Hames, O., Jafari, M., & Lehning, M. (2021). snowBedFoam: An OpenFOAM Eulerian-Lagrangian solver for modelling snow transport (version 1.0) [Software]. *EnviDat*. https://doi.org/10.16904/envidat.223

Hancock, H., Eckerstorfer, M., Prokop, A., & Hendrikx, J. (2020). Quantifying seasonal cornice dynamics using a terrestrial laser scanner in Svalbard, Norway. *Natural Hazards and Earth System Sciences*, *20*(2), 603–623. https://doi.org/10.5194/nhess-20-603-2020

Kok, J. F., & Renno, N. O. (2009). A comprehensive numerical model of steady state saltation (comsalt). *Journal of Geophysical Research*, *114*(D17), D17204. https://doi.org/10.1029/2009jd011702

Latham, J., & Montagne, J. (1970). The possible importance of electrical forces in the development of snow cornices. *Journal of Glaciology*, *9*(57), 375–384. (Publisher: Cambridge University Press). https://doi.org/10.3189/s0022143000022899

Lu, H., & Zhang, L.-z. (2019). Effects of blockage ratio and Reynolds number on particle deposition in duct airflow over a forward-facing step. *Building Simulation*, *12*(6), 1119–1129. https://doi.org/10.1007/s12273-019-0544-2

Melo, D. B., Sharma, V., Comola, F., Sigmund, A., & Lehning, M. (2022). Modeling snow saltation: The effect of grain size and interparticle cohesion. *Journal of Geophysical Research: Atmospheres*, *127*(1), e2021JD035260. (Publisher: Wiley Online Library). https://doi.org/10.1029/2021jd035260

Mott, R., Schirmer, M., Bavay, M., Grünewald, T., & Lehning, M. (2010). Understanding snow-transport processes shaping the mountain snow-cover. *The Cryosphere*, *4*(4), 545–559. https://doi.org/10.5194/tc-4-545-2010

Nemoto, M., & Nishumura, K. (2001). Direct measurement of shear stress during snow saltation. *Boundary-Layer Meteorology*, *100*(1), 149–170. https://doi.org/10.1023/A:1019267015986

Seligman, G., Seligman, G. A., & Douglas, C. (1936). *Snow structure and ski fields: Being an account of snow and ice forms met with in nature, and a study on avalanches and snowcraft*. Macmillan and Company, Limited.

Sharma, V., Comola, F., & Lehning, M. (2018). On the suitability of the thorpe–mason model for calculating sublimation of saltating snow. *The Cryosphere*, *12*(11), 3499–3509. https://doi.org/10.5194/tc-12-3499-2018

Sommer, C. G., Lehning, M., & Fierz, C. (2017). Wind tunnel experiments: Saltation is necessary for wind-packing. *Journal of Glaciology*, *63*(242), 950–958. https://doi.org/10.1017/jog.2017.53

Szabo, D., & Schneebeli, M. (2007). Subsecond sintering of ice. *Applied Physics Letters*, *90*(15), 151916. https://doi.org/10.1063/1.2721391

Vogel, S., Eckerstorfer, M., & Christiansen, H. H. (2012). Cornice dynamics and meteorological control at Gruvefjellet, Central Svalbard. *The Cryosphere*, *6*(1), 157–171. https://doi.org/10.5194/tc-6-157-2012

Yu, H. (2024). Numerical simulation of snow cornice formation [Dataset]. *Zenodo*. https://doi.org/10.5281/zenodo.13997845

Yu, H., Lehning, M., Li, G., Walter, B., Huang, J., & Huang, N. (2024). Snow particle motion in process of cornice formation. *EGUsphere*, *2024*, 1–15. https://doi.org/10.5194/egusphere-2024-2458

Yu, H., Li, G., Walter, B., Lehning, M., Zhang, J., & Huang, N. (2022). Environmental conditions for snow cornice formation tested in a wind tunnel. *The Cryosphere*, 1–15. https://doi.org/10.5194/tc-2022-27

Zhang, Y., Yue, K., Zhang, X., & Zhang, X. (2023). Deposition characteristics of particles in backward-facing step flow and a radiant syngas cooler. *Case Studies in Thermal Engineering*, *43*, 102799. https://doi.org/10.1016/j.csite.2023.102799